Integrated radial basis function networks for computing Newtonian and non-Newtonian fluid flows

N. Mai-Duy* and T. Tran-Cong

Computational Engineering and Science Research Centre

Faculty of Engineering and Surveying,

The University of Southern Queensland, Toowoomba, QLD 4350, Australia

Submitted to *Computers and Structures*, 19-May-2008; revised 14-Aug-2008

*Corresponding author: Telephone +61 7 4631 1324, Fax +61 7 4631 2526, E-mail maiduy@usq.edu.au

Abstract: This paper presents a radial-basis-function (RBF) collocation method for the simulation of two-dimensional fluid-flow problems. To improve the stability of a discrete solution and the quality of derivative approximations, the present RBF networks (RBFNs) are constructed through integration instead of conventional differentiation. Special attention is given to the following two topics: (i) the effective use of integration constants in the solution of the Navier-Stokes equations and (ii) the employment of "local" integrated RBFNs to handle flows with fine structures. Different types of geometries and fluids are considered. The accuracy of the present technique is demonstrated through the solution of several benchmark test problems.

Keywords: radial-basis-function networks, integral collocation formulation, Navier-Stokes equations

1 Introduction

Radial-basis-function networks (RBFNs) are known as a powerful numerical tool for the approximation of scattered data. Theoretical results [1] show that the RBF interpolation matrix is nonsingular, whatever the number of the data sites. RBFNs have the property of universal approximation; they can approximate arbitrarily-well continuous functions. Moreover, a number of RBFs such as the multiquadric and Gaussian basis functions exhibit an exponential rate of convergence. Over the past 15 years, RBFNs have very successfully been used for the solution of partial differential equations (PDEs) (e.g. [2,3]). Unlike low-order discretisation techniques such as finite-difference and finite-element methods, RBF collocation methods are capable of providing very accurate results using a relatively-small number of data points. In contrast to pseudo spectral techniques, they can work with arbitrarily-scattered data. On the other hand, the resultant RBF systems are dense and they

are generally ill-conditioned, which can limit the use of RBFNs to discrete systems with a few hundred points. In addition, theories for determining the optimal values for the RBFN parameters, for example the RBF width and centre, are still lacking. It is still difficult to achieve spectral accuracy in practice. Considerable effort has been put into developing techniques to overcome these difficulties. A comprehensive discussion on RBF-based methods can be found in [4].

As shown in [5] (Theorem 4.4), the accuracy for approximating a derivative by conventional (differentiated) RBFNs (DRBFNs) is a decreasing function of derivative order. It is expected that this deterioration of accuracy is avoided by constructing the RBF approximations through integration. Mai-Duy and Tran-Cong [6,7] have proposed the use of integrated RBFNs (IRBFNs) for the representation of a given function and the solution of a PDE. The highest derivatives under consideration are decomposed into RBFs; expressions for lower derivatives and the function itself are then obtained through integration. Numerical studies have shown that the integral formulation is more accurate than the differential formulation. Recently, theoretical studies [8] have confirmed superior accuracy of IRBFNs over DRBFNs. Moreover, there are additional weights (integration constants) in the integral collocation formulation, and they have been found to be extremely useful for handling the multiple boundary conditions [9,10,11]. IRBFN solutions to various differential problems have been reported (e.g. [12-15]).

To employ a larger number of collocation points, a numerical scheme based on one-dimensional IRBFNs has been proposed recently [16,17]. A problem domain, which can be regular or irregular, is embedded in a rectangular domain and it is then discretised using a Cartesian grid, i.e. an array of straight lines that run parallel to the $x-$ and $y-$axes. The interior points are defined as grid points inside the problem domain, while the boundary points are generated by the intersection of the grid lines with boundaries. Grid nodes outside the problem domain are removed

from the computations. It can be seen that the preprocessing of this numerical scheme is economical. The governing equations can be of complicated forms such as those involving high-order and cross derivatives. Let the domain be rectangular and N_x and N_y be the numbers of grid lines in the $x-$ and $y-$directions, respectively. On a grid line, IRBFNs are employed to represent the field variable and its relevant derivatives. The construction for the approximations at a point involves a number of N_x or N_y points rather than the usual N_xN_y points. The 1D-IRBFN approach leads to a considerable improvement in the matrix condition number and computational effort over the 2D-IRBFN approach. It is expected that extension to 3D problems can be carried out straightforwardly.

This paper is concerned with the use of IRBFNs for the simulation of 2D steady incompressible flow problems. The motion of a fluid can be described by the equations of conservation of mass, momentum and energy. The continuity and momentum equations may be formulated in terms of: (i) velocity and pressure, (ii) stream function and vorticity, and (iii) stream function. The last two formulations, which are adopted here, are attractive because, first, the pressure does not have to be considered, which results in computational efficiency and ease of implementation; second, the number of equations to be solved is reduced; and third, the continuity equation is automatically satisfied. However, there is the need to derive boundary conditions for the vorticity variable if one uses the stream function and vorticity formulation, and to implement double boundary conditions if one chooses the stream-function formulation. It will be shown that the integral collocation formulation provides an effective way to handle these issues. Since the structure of a flow is usually complex, a sufficiently large number of nodes is required for an accurate simulation. We prefer to use 1D-IRBFNs ("local" approximations) to simulate fluid-flow problems in two dimensions.

The remainder of the paper is organised as follows. Section 2 briefly outlines 1D-

IRBFNs. In section 3, the 1D-IRBFN collocation technique is presented through the simulation of lid-driven and thermally-driven viscous flows and non-rectilinear viscoelastic flows. Results are compared with benchmark solutions, where appropriate. Section 4 concludes the paper.

2 One-dimensional integrated RBFNs

Consider a univariate function $f(x)$. The basic idea of the integral RBF scheme [6] is to decompose a pth-order derivative of the function f into RBFs

$$\frac{d^p f(x)}{dx^p} = \sum_{i=1}^{N_x} w_i \varphi_i(x) = \sum_{i=1}^{N_x} w_i I_i^{(p)}(x), \tag{1}$$

where $\{w_i\}_{i=1}^{N_x}$ is the set of network weights, and $\{\varphi_i(x)\}_{i=1}^{N_x} \equiv \left\{I_i^{(p)}(x)\right\}_{i=1}^{N_x}$ is the set of RBFs. Lower-order derivatives and the function itself are then obtained through integration

$$\frac{d^{p-1} f(x)}{dx^{p-1}} = \sum_{i=1}^{N_x} w_i I_i^{(p-1)}(x) + c_1, \tag{2}$$

$$\frac{d^{p-2} f(x)}{dx^{p-2}} = \sum_{i=1}^{N_x} w_i I_i^{(p-2)}(x) + c_1 x + c_2, \tag{3}$$

$$\cdots \quad \cdots \qquad \cdots \qquad \cdots \qquad \cdots$$

$$\frac{df(x)}{dx} = \sum_{i=1}^{N_x} w_i I_i^{(1)}(x) + c_1 \frac{x^{p-2}}{(p-2)!} + c_2 \frac{x^{p-3}}{(p-3)!} + \cdots + c_{p-2} x + c_{p-1}, \tag{4}$$

$$f(x) = \sum_{i=1}^{N_x} w_i I_i^{(0)}(x) + c_1 \frac{x^{p-1}}{(p-1)!} + c_2 \frac{x^{p-2}}{(p-2)!} + \cdots + c_{p-1} x + c_p, \tag{5}$$

where $I_i^{(p-1)}(x) = \int I_i^{(p)}(x)dx$, $I_i^{(p-2)}(x) = \int I_i^{(p-1)}(x)dx, \cdots, I_i^{(0)}(x) = \int I_i^{(1)}(x)dx$, and $(c_1, c_2, \cdots, c_p)$ are the constants of integration.

Unlike conventional differential schemes, the starting point of the integral scheme can vary in use, depending on the particular application under consideration. The scheme is said to be of order p, denoted by IRBFN-p, if the pth-order derivative is taken as the starting point.

Evaluation of (1)-(5) at a set of collocation points $\{x_i\}_{i=1}^{N_x}$ leads to

$$\widehat{\frac{d^p f}{dx^p}} = \widehat{\mathcal{I}}_{[p]}^{(p)} \widehat{\alpha}, \tag{6}$$

$$\widehat{\frac{d^{p-1} f}{dx^{p-1}}} = \widehat{\mathcal{I}}_{[p]}^{(p-1)} \widehat{\alpha}, \tag{7}$$

$$\cdots\cdots\cdots$$

$$\widehat{\frac{df}{dx}} = \widehat{\mathcal{I}}_{[p]}^{(1)} \widehat{\alpha}, \tag{8}$$

$$\widehat{f} = \widehat{\mathcal{I}}_{[p]}^{(0)} \widehat{\alpha}, \tag{9}$$

where the subscript [.] and superscript (.) are used to denote the order of an IRBFN scheme and the order of a derivative function, respectively;

$$\widehat{\mathcal{I}}_{[p]}^{(p)} = \begin{bmatrix} I_1^{(p)}(x_1), & I_2^{(p)}(x_1), & \cdots, & I_{N_x}^{(p)}(x_1), & 0, & 0, & \cdots, & 0, & 0 \\ I_1^{(p)}(x_2), & I_2^{(p)}(x_2), & \cdots, & I_{N_x}^{(p)}(x_2), & 0, & 0, & \cdots, & 0, & 0 \\ \vdots & \vdots & \vdots & \vdots & \vdots & \vdots & \ddots & \vdots & \vdots \\ I_1^{(p)}(x_{N_x}), & I_2^{(p)}(x_{N_x}), & \cdots, & I_{N_x}^{(p)}(x_{N_x}), & 0, & 0, & \cdots, & 0, & 0 \end{bmatrix},$$

$$\widehat{\mathcal{I}}_{[p]}^{(p-1)} = \begin{bmatrix} I_1^{(p-1)}(x_1), & I_2^{(p-1)}(x_1), & \cdots, & I_{N_x}^{(p-1)}(x_1), & 1, & 0, & \cdots, & 0, & 0 \\ I_1^{(p-1)}(x_2), & I_2^{(p-1)}(x_2), & \cdots, & I_{N_x}^{(p-1)}(x_2), & 1, & 0, & \cdots, & 0, & 0 \\ \vdots & \vdots & \vdots & \vdots & \vdots & \vdots & \ddots & \vdots & \vdots \\ I_1^{(p-1)}(x_{N_x}), & I_2^{(p-1)}(x_{N_x}), & \cdots, & I_{N_x}^{(p-1)}(x_{N_x}), & 1, & 0, & \cdots, & 0, & 0 \end{bmatrix},$$

$\cdots\cdots$,

$$\widehat{\mathcal{I}}^{(0)}_{[p]} = \begin{bmatrix} I^{(0)}_1(x_1), & I^{(0)}_2(x_1), & \cdots, & I^{(0)}_{N_x}(x_1), & \frac{x_1^{p-1}}{(p-1)!}, & \frac{x_1^{p-2}}{(p-2)!}, & \cdots, & x_1, & 1 \\ I^{(0)}_1(x_2), & I^{(0)}_2(x_2), & \cdots, & I^{(0)}_{N_x}(x_2), & \frac{x_2^{p-1}}{(p-1)!}, & \frac{x_2^{p-2}}{(p-2)!}, & \cdots, & x_2, & 1 \\ \vdots & \vdots & \vdots & \vdots & \vdots & \vdots & \ddots & \vdots & \vdots \\ I^{(0)}_1(x_{N_x}), & I^{(0)}_2(x_{N_x}), & \cdots, & I^{(0)}_{N_x}(x_{N_x}), & \frac{x_{N_x}^{p-1}}{(p-1)!}, & \frac{x_{N_x}^{p-2}}{(p-2)!}, & \cdots, & x_{N_x}, & 1 \end{bmatrix};$$

$$\widehat{\alpha} = (w_1, w_2, \cdots, w_{N_x}, c_1, c_2, \cdots, c_p)^T;$$

and

$$\widehat{\frac{d^k f}{dx^k}} = \left(\frac{d^k f_1}{dx^k}, \frac{d^k f_2}{dx^k}, \cdots, \frac{d^k f_{N_x}}{dx^k}\right)^T, \quad k = (1, 2, \cdots, p),$$
$$\widehat{f} = (f_1, f_2, \cdots, f_{N_x})^T,$$

in which $d^k f_i/dx^k = d^k f(x_i)/dx^k$ and $f_i = f(x_i)$ with $i = (1, 2, \cdots, N_x)$.

3 Present 1D-IRBFN collocation technique

1D-IRBFNs are implemented to simulate several benchmark problems. The first problem is a lid-driven cavity viscous flow, where the moving lid introduces a singularity. The discontinuous velocity and the boundless vorticity in the upper corners present a great numerical challenge especially for high-order discretisation techniques. We solve the set of equations written in the stream function and vorticity variables. A new technique for deriving boundary conditions for the vorticity is presented. The second problem is a natural convection flow between confocal horizontal elliptical cylinders, where the velocity and temperature fields are closely coupled. The problem domain is multiply connected. There are more equations to be solved simultaneously, making the numerical analysis more difficult. We take the stream

function formulation as the governing equation and special emphasis is placed on the implementation of double boundary conditions. The last problem is a fully-developed flow of a viscoelastic fluid in a square duct. Further computational effort is required to obtain viscoelastic stresses that involve high-order derivatives. All simulations are performed with the multiquadric (MQ) basis function whose form is

$$\varphi_i(x) = \sqrt{(x - c_i)^2 + a_i^2}, \tag{10}$$

where c_i and a_i are the MQ centre and width, respectively. The present MQ width is simply chosen to be the grid size, and the two sets of centres $\{c_i\}_{i=1}^{N_x}$ and collocation points $\{x_i\}_{i=1}^{N_x}$ are identical. The simultaneous linear algebraic equations obtained are simply solved using standard algorithms available in the literature such as those provided in MATLAB.

3.1 Lid-driven cavity viscous flow

The governing equations employed here are the Navier-Stokes equations written in the stream function ψ and vorticity ω as

$$\frac{\partial \omega}{\partial t} + \left(\frac{\partial \psi}{\partial y} \frac{\partial \omega}{\partial x} - \frac{\partial \psi}{\partial x} \frac{\partial \omega}{\partial y} \right) = \frac{1}{R_e} \left(\frac{\partial^2 \omega}{\partial x^2} + \frac{\partial^2 \omega}{\partial y^2} \right), \tag{11}$$

$$-\omega = \frac{\partial^2 \psi}{\partial x^2} + \frac{\partial^2 \psi}{\partial y^2}, \tag{12}$$

where R_e is the Reynolds number, t the time, and $(x, y)^T$ the position vector.

The x and y components of the velocity vector are defined in terms of stream function as

$$u = \frac{\partial \psi}{\partial y}, \quad v = -\frac{\partial \psi}{\partial x}. \tag{13}$$

The cavity is taken to be a unit square, with the lid sliding from left to right at a

unit velocity. The boundary conditions for u and v become

$$\psi = 0,\ \frac{\partial \psi}{\partial x} = 0, \qquad x = 0,\ x = 1, \tag{14}$$

$$\psi = 0,\ \frac{\partial \psi}{\partial y} = 0, \qquad y = 0, \tag{15}$$

$$\psi = 0,\ \frac{\partial \psi}{\partial y} = 1, \qquad y = 1. \tag{16}$$

The domain is discretised using a uniform Cartesian grid. The stream function and vorticity on a grid line are represented by 1D-IRBFN-2s. We will find ψ and ω in terms of their nodal values. For a grid line, the relations between the network weights including two integration constants ($\widehat{\alpha}$) and the nodal variable values ($\widehat{f}$) can be described by

$$\widehat{f} = \widehat{\mathcal{I}}^{(0)}_{[2]}\widehat{\alpha} = \widehat{\mathcal{C}}\widehat{\alpha}, \tag{17}$$

$$\widehat{\alpha} = \widehat{\mathcal{C}}^{-1}\widehat{f}, \tag{18}$$

where $\widehat{f}$, $\widehat{\alpha}$ and $\widehat{\mathcal{I}}^{(0)}_{[2]}$ are defined as before, $\widehat{\mathcal{C}}^{-1}$ is the pseudo inverse of the conversion matrix $\widehat{\mathcal{C}}$. It is noted that f represents ψ and ω.

Using (1)-(4) with $p = 2$ and (18), the values of derivatives of f at a grid point (x_i, y_j) can be computed by

$$\frac{\partial f(x_i, y_j)}{\partial x} = \left[I_1^{(1)}(x_i), I_2^{(1)}(x_i), \cdots, I_{N_x}^{(1)}(x_i), 1, 0\right]\widehat{\mathcal{C}}^{-1}\widehat{f}_i, \tag{19}$$

$$\frac{\partial^2 f(x_i, y_j)}{\partial x^2} = \left[I_1^{(2)}(x_i), I_2^{(2)}(x_i), \cdots, I_{N_x}^{(2)}(x_i), 0, 0\right]\widehat{\mathcal{C}}^{-1}\widehat{f}_i, \tag{20}$$

$$\frac{\partial f(x_i, y_j)}{\partial y} = \left[I_1^{(1)}(y_j), I_2^{(1)}(y_j), \cdots, I_{N_y}^{(1)}(y_j), 1, 0\right]\widehat{\mathcal{C}}^{-1}\widehat{f}_j, \tag{21}$$

$$\frac{\partial^2 f(x_i, y_j)}{\partial y^2} = \left[I_1^{(2)}(y_j), I_2^{(2)}(y_j), \cdots, I_{N_y}^{(2)}(y_j), 0, 0\right]\widehat{\mathcal{C}}^{-1}\widehat{f}_j, \tag{22}$$

where $\widehat{f}_i$ and $\widehat{f}_j$ are the vectors whose entries are the nodal values of f on the grid line $y = y_j$ and $x = x_i$, respectively. We thus express derivatives of f in terms of

its nodal values. Assume that the variable f is prescribed on the boundaries. To find its interior values, a number of algebraic equations that is equal to a number of unknowns needs to be generated. This can be achieved by collocating the governing differential equation at the interior points. The assembly of 1D-IRBFNs to obtain the equations of the entire domain is similar to those of conventional discretisation techniques.

From (14)-(16), it can be seen that the boundary conditions are over-prescribed for (12), but under-prescribed for (11). The Dirichlet boundary conditions, ψ, are used for solving (12), while the Neumann boundary conditions, $\partial\psi/\partial n$ (i.e. $\partial\psi/\partial n = \nabla\psi.\widehat{n}$, where $\widehat{n}$ is the outward unit normal vector at a point on the boundary), are used to derive computational boundary conditions for ω for solving (11). Making use of (12), the values of ω on the boundaries are computed by

$$\omega = -\frac{\partial^2\psi}{\partial x^2} = -\sum_{i=1}^{N_x} w_i I_i^{(2)}(x), \qquad x = 0 \text{ and } x = 1, \tag{23}$$

$$\omega = -\frac{\partial^2\psi}{\partial y^2} = -\sum_{j=1}^{N_y} w_j I_j^{(2)}(y), \qquad y = 0 \text{ and } y = 1. \tag{24}$$

In computing (23) and (24), one needs to incorporate $\partial\psi/\partial x$ into $\partial^2\psi/\partial x^2$ and $\partial\psi/\partial y$ into $\partial^2\psi/\partial y^2$, respectively. We present a new technique to derive the boundary values for ω. Since $\widehat{\alpha}$ includes two integration constants (i.e. two extra coefficients), one can add two additional equations representing the Neumann boundary conditions to the conversion system, for example for the one associated with a horizontal line, as

$$\begin{pmatrix} \widehat{\psi} \\ \frac{\partial\psi_1}{\partial x} \\ \frac{\partial\psi_{N_x}}{\partial x} \end{pmatrix} = \begin{bmatrix} \mathcal{I}_{[2]}^{(0)} \\ \mathcal{K} \end{bmatrix} \widehat{\alpha} = \mathcal{C}\widehat{\alpha}, \tag{25}$$

where $\mathcal{K}$ is the matrix made up of the first and last rows of $\widehat{\mathcal{I}}_{[2]}^{(1)}$, and the conversion matrix $\mathcal{C}$ is of dimension $(N_x+2)\times(N_x+2)$. The computational boundary condition

(23) becomes

$$\omega = \left[I_1^{(2)}(x), I_2^{(2)}(x), \cdots, I_{N_x}^{(2)}(x), 0, 0 \right] \widehat{\mathcal{C}}^{-1} \begin{pmatrix} \widehat{\psi} \\ \frac{\partial \psi_1}{\partial x} \\ \frac{\partial \psi_{N_x}}{\partial x} \end{pmatrix} \tag{26}$$

that contains derivative information on the walls. In this implementation, the boundary approximations have the same order as the interior approximations, and all nodal values of ψ are taken into account.

We are interested only in the final steady state of the flow. The resultant system of nonlinear algebraic equations is solved using the following iterative procedure.

1. Guess the initial solution
2. Solve (12) for ψ
3. Compute the boundary values for ω and the convective terms
4. Solve (11) for ω, where the time derivative term is discretised using a first-order Euler scheme and the diffusive terms are treated implicitly
5. Check convergence for ω

$$\frac{\sqrt{\sum_{i=1}^{N} \left(\omega_i^{(k)} - \omega_i^{(k-1)} \right)^2}}{\sqrt{\sum_{i=1}^{N} \left(\omega_i^{(k)} \right)^2}} < 10^{-9}, \tag{27}$$

where k is the time level. If not converged, advance time step and return to step 2. Otherwise, stop.

A wide range of R_e, namely (100, 400, 1000, 3200), is considered. Convergence is studied using 10 uniform grids: 11×11, $21 \times 21, \cdots, 101 \times 101$. In solving (11),

we use time steps varying from 0.1 to 0.0005. Smaller time steps are employed for higher Res and denser grid densities.

The lid-driven cavity flow is usually used as a test problem for the assessment of accuracy of numerical solvers in CFD. Results by Ghia, Ghia and Shin [18] using a finite-difference discretisation with a dense grid are widely considered as a benchmark solution. Recently, Botella and Peyret [19] have decomposed the field variable into the regular and singular parts. The former is determined using a pseudo spectral technique, while the latter is treated analytically. A benchmark spectral solution is provided for $R_e = 1000$, where convergence is achieved up to seven digits. The IRBFN results are compared with the benchmark finite-difference and spectral solutions and some other solutions reported in the literature in Table 1 for velocity and in Table 2 for stream function and vorticity. It can be seen that the present results are in better agreement with the spectral solutions, even at relatively coarse grids. Some contour plots for $R_e = 1000$ and $R_e = 3200$ are shown in Figure 1. When compared with pseudo spectral techniques, attractive features of the present global technique are that it does not require any special treatments for the corner singularity and it can work with uniform grids.

3.2 Thermally-driven viscous flow

Natural convection between confocal horizontal elliptical cylinders with isothermal surfaces is considered. The governing equations are taken to be in the temperature

and stream function formulation as [21]

$$\frac{\partial T}{\partial t}+\frac{\partial \psi}{\partial y}\frac{\partial T}{\partial x}-\frac{\partial \psi}{\partial x}\frac{\partial T}{\partial y}=\frac{1}{\sqrt{RaPr}}\left(\frac{\partial^2 T}{\partial x^2}+\frac{\partial^2 T}{\partial y^2}\right), \tag{28}$$

$$\frac{\partial}{\partial t}\left(\frac{\partial^2 \psi}{\partial x^2}+\frac{\partial^2 \psi}{\partial y^2}\right)+\frac{\partial \psi}{\partial y}\left(\frac{\partial^3 \psi}{\partial x^3}+\frac{\partial^3 \psi}{\partial x \partial y^2}\right)-\frac{\partial \psi}{\partial x}\left(\frac{\partial^3 \psi}{\partial x^2 \partial y}+\frac{\partial^3 \psi}{\partial y^3}\right)+\frac{\partial T}{\partial x}=$$
$$\sqrt{\frac{Pr}{Ra}}\left(\frac{\partial^4 \psi}{\partial x^4}+2\frac{\partial^4 \psi}{\partial x^2 \partial y^2}+\frac{\partial^4 \psi}{\partial y^4}\right), \tag{29}$$

where T is the temperature, P_r the Prandtl number, and R_a the Rayleigh number.

The boundary conditions are prescribed as $\psi = 0$ and $\partial\psi/\partial n = 0$ on all the boundaries, $T = 0$ on the outer surface, and $T = 1$ on the inner surface.

The dimensionless geometrical parameters of the problem can be defined as [22]

$$a_i = \frac{1}{(rr-1)(1-e_i^2)^{1/4}}, \quad b_i = \frac{(1-e_i^2)^{1/4}}{rr-1}, \tag{30}$$

$$a_o = \frac{rr}{(rr-1)(1-e_o^2)^{1/4}}, \quad b_o = \frac{rr(1-e_i^2)^{1/4}}{rr-1}, \tag{31}$$

where a and b represent the semimajor and semiminor axes; e denotes the eccentricity ($e = \sqrt{a^2-b^2}/a$); the subscripts o and i refer to the outer and inner ellipses; and $rr = \sqrt{a_o b_o / a_i b_i}$.

For this flow, one important measurement is the average Nusselt number defined as

$$\overline{N_u} = -\frac{1}{2\pi}\int_{\theta=-\pi}^{\theta=+\pi}\frac{\partial T}{\partial n}d\theta \tag{32}$$

where $\partial T/\partial n$ is the normal derivative of T on the inner surface.

In contrast to horizontal circular annuli, there are relatively few papers on elliptical cylinders. Works reported include [23,24,25,22]. Zhu et al [22] studied this problem for $R_a = 10^4$ and 68 different physical domains using the differential quadrature

(DQ) method. The non-rectangular physical domain is transformed into the rectangular computational domain. They employed a Fourier series expansion with uniform points to represent the derivatives in the circumferential direction, and an algebraic polynomial with cosine-type points to discretise the derivatives in the radial direction. The governing equations are solved in the stream function, vorticity and temperature formulation. Grid convergence study is reported for the case of $rr = 2.6$, $e_i = 0.5$ and $e_o = 0.5$. Since spectral approximations are very accurate (exponential convergence), Zhu et al's results are used here to provide a useful basis for the assessment of accuracy of the present method.

The problem domain is presently embedded in a Cartesian grid (Figure 2). On a grid line, we employ 1D-IRBFN-2s and 1D-IRBFN-4s to represent the temperature and stream function, respectively. Because of no underlying mesh required, 1D-IRBFNs can work with regular and irregular boundary points in a similar fashion. The discretisation process for T is the same as that for ψ and ω in the previous problem. Emphasis is placed on the IRBFN solution of (29) (fourth-order PDE) that is subject to double boundary conditions. From the prescribed values ψ and $\partial\psi/\partial n$, one can easily derive the values of $\partial\psi/\partial x$ and $\partial\psi/\partial y$ on the surfaces. The derivative boundary conditions are implemented through the process of converting the RBF weight spaces into the physical space. On a grid line, e.g. a horizontal one, one can construct the following system

$$\begin{pmatrix} \widehat{\psi} \\ \frac{\partial \psi_1}{\partial x} \\ \frac{\partial \psi_{N_x}}{\partial x} \end{pmatrix} = \begin{bmatrix} \mathcal{I}_{[4]}^{(0)} \\ \mathcal{K} \end{bmatrix} \widehat{\alpha} = \mathcal{C}\widehat{\alpha}, \tag{33}$$

where $\mathcal{K}$ is the matrix made up of the first and last rows of $\widehat{\mathcal{I}}_{[4]}^{(1)}$. The mixed

derivatives in (29) are computed according to

$$\frac{\partial^3 \psi}{\partial x^2 \partial y} = \frac{\partial^2}{\partial x^2}\left(\frac{\partial \psi}{\partial y}\right), \tag{34}$$

$$\frac{\partial^3 \psi}{\partial x \partial y^2} = \frac{\partial^2}{\partial y^2}\left(\frac{\partial \psi}{\partial x}\right), \tag{35}$$

$$\frac{\partial^4 \psi}{\partial x^2 \partial y^2} = \frac{1}{2}\left[\frac{\partial^2}{\partial x^2}\left(\frac{\partial^2 \psi}{\partial y^2}\right) + \frac{\partial^2}{\partial y^2}\left(\frac{\partial^2 \psi}{\partial x^2}\right)\right], \tag{36}$$

where the computation of the cross derivative is replaced with that of pure lower-order derivatives. It is noted that the differential operators $\partial^2()/\partial x^2$ and $\partial^2()/\partial y^2$ in (34)-(36) are approximated using 1D-IRBFN-2s. After the conversion processes are carried out, the 1D-IRBFN approximations include information about the boundary conditions. One thus need to force those approximations to satisfy the governing equations only. This can be achieved by collocating (28) and (29) at the interior points.

To obtain the structure of a steady flow with the working fluid being air ($P_r = 0.71$), we compute the solution of a transient flow problem until a steady state is established. The solution procedure is thus similar to that in the previous problem. At each time step, the temperature and stream function problems are solved as separate systems in order to minimise the matrix size. We employ several Cartesian grids, varying from 37×37 to 57×57 and a time step of 0.1. Grid independent study is conducted through the average Nusselt number and the obtained results are shown in Table 3. It can be seen that the computed $\overline{N_u}$ remains unchanged when the grid is above 41×41. The difference of the grid independent value between the 1D-IRBFN and DQ methods is less than 1%. Streamlines and isotherms for two typical domains are presented in Figure 3. They look feasible when compared to those in [22]. The corresponding values of $\overline{N_u}$ are 3.48 and 3.29 using a grid of 57×57, which are in good agreement with the DQ method's results (3.50 and 3.30, respectively). For the former, where the orientation of the major axis of the outer

ellipse is placed horizontally, there are two additional vortices.

The present technique has several advantages over the finite-difference and pseudo spectral methods: (i) the governing equations are solved in Cartesian coordinates (no coordinate transformations are required), and (ii) the boundary conditions are imposed in an exact manner (no assumption of uniform vorticity is made here, which is in contrast to [25], and all nodal variable values are taken into account for the implementation of boundary conditions).

3.3 Fully developed viscoelastic flow in a square duct

The flow behaviour of viscoelastic fluid in straight pipes of arbitrary cross-sectional shape has received much attention. In contrast to Newtonian flows, viscoelastic flows may contain some weak secondary circulations. The pathlines of a fluid are thus not straight. Such non-rectilinear motions arise from the fact that viscoelastic fluids exhibit normal stress differences in a simple shearing flow. The present work is concerned with the case of square cross section. The working fluid is modelled by the CEF equation [26]

$$\boldsymbol{\tau} = \eta(\dot{\gamma})\dot{\boldsymbol{\gamma}} + \left(\frac{1}{2}\Psi_1 + \Psi_2\right)(\dot{\boldsymbol{\gamma}}.\dot{\boldsymbol{\gamma}}) - \frac{1}{2}\Psi_1\frac{\mathcal{D}\dot{\boldsymbol{\gamma}}}{\mathcal{D}t}, \tag{37}$$

where $\boldsymbol{\tau}$ is the extra stress tensor; $\eta(\dot{\gamma})$ the viscosity; $\dot{\boldsymbol{\gamma}}$ the rate of deformation tensor; $\dot{\gamma}$ the scalar magnitude of $\dot{\boldsymbol{\gamma}}$; Ψ_1 and Ψ_2 the first and second normal stress coefficients, respectively; and $\mathcal{D}\dot{\boldsymbol{\gamma}}/\mathcal{D}t$ the corotational derivative.

To enhance numerical stability, the extra stress tensor is decomposed into

$$\boldsymbol{\tau} = \eta_0\boldsymbol{\tau} + \mathbf{S} \tag{38}$$

where $\mathbf{S} = (\boldsymbol{\tau} - \eta_0 \boldsymbol{\tau})$. It is obvious that η_0 can be chosen arbitrarily. The governing equations are taken in the following form

$$0 = \frac{\partial^2 \psi}{\partial x^2} + \frac{\partial^2 \psi}{\partial y^2} + \omega, \tag{39}$$

$$\rho \left(\frac{\partial \psi}{\partial y} \frac{\partial \omega}{\partial x} - \frac{\partial \psi}{\partial x} \frac{\partial \omega}{\partial y} \right) - \frac{\partial^2 S_{xy}}{\partial x^2} + \frac{\partial^2 (S_{xx} - S_{yy})}{\partial x \partial y} + \frac{\partial^2 S_{xy}}{\partial y^2} = \eta_0 \left(\frac{\partial^2 \omega}{\partial x^2} + \frac{\partial^2 \omega}{\partial y^2} \right), \tag{40}$$

$$\frac{\partial p}{\partial z} + \rho \left(\frac{\partial \psi}{\partial y} \frac{\partial v_z}{\partial x} - \frac{\partial \psi}{\partial x} \frac{\partial v_z}{\partial y} \right) - \frac{\partial S_{zx}}{\partial x} - \frac{\partial S_{zy}}{\partial y} = \eta_0 \left(\frac{\partial^2 v_z}{\partial x^2} + \frac{\partial^2 v_z}{\partial y^2} \right), \tag{41}$$

with homogeneous boundary conditions for ψ, $\partial \psi / \partial n$ and v_z. The present work employs the same geometry (the size of the cross section) and rheological model as in [27]. The flows in the pipe are generated by a pressure drop $\partial p / \partial z$. 1D-IRBFN-2s are implemented to obtain the primary and secondary flows. We take $\psi = 0$ and $v_z = 0$ as the boundary conditions for (39) and (41), respectively. For (40), boundary conditions for ω are derived from (39) and derivative information on the walls ($\partial \psi / \partial n = 0$), which takes the same procedure as in the lid-driven cavity flow problem. The computations are carried out using a grid of 41×41. The stress components are straightforwardly computed from the velocity field as their forms are given explicitly in (37). It is noted that pseudo body forces in (40) involve pure and cross derivatives of orders up to four. We solve the resultant system of nonlinear algebraic equations with a Picard iterative scheme, where a relaxation factor of 0.005 is used. The value of η_0 is taken to be the average of the viscosity field from the previous iteration. Numerical experiments showed that such a choice produces a faster and stabler iterative procedure than the usual choice of a fixed value (e.g. the Newtonian-like viscosity). Figure 4 shows the patterns of the primary and secondary flows together with the second normal stress difference. It clearly indicates the existence of two counter-rotating vortices in each quadrant of the pipe, which looks feasible when compared with existing results from different

methods reported in the literature (e.g. [27,28]).

3.4 Discussion

3.4.1 Comparison with conventional RBF techniques

The present RBF approximations are constructed "locally". They only involve nodal points on relevant grid lines rather than a whole set of points. As a result, the obtained system matrix becomes sparse. Numerical experiments indicate a very significant improvement in the matrix condition number.

3.4.2 Comparison with principal discretisation techniques

Unlike pseudo-spectral and finite-difference methods, the present Cartesian-grid technique can handle irregular domains well. In contrast to finite elements and finite volumes, the pre-processing here is much more economical. The problem domain is discretised using a set of grid lines that are parallel to the $x-$ and $y-$axes instead of a set of small elements. When compared with low order techniques, the present technique can produce accurate results on a relatively coarse mesh, therefore has the ability to reduce a computational effort for a given accuracy. On the other hand, with more points (i.e. all nodes on a grid line) used, the cost to construct the approximations here is much higher. In addition, the present system matrix is not as sparse as those obtained with finite differences, finite elements and finite volumes. However, the system matrix would be block-banded when domain decomposition is employed. The IRBFN-based methods have been shown in [29] to have definite advantage in terms of accuracy and stability owing to its ability to ensure C^p solutions, where p is the order of the governing PDEs, across subdomain interfaces. In

order to achieve highly-stable numerical schemes for the simulation of viscous flows at high Reynolds numbers such as those reported by Bathe and co-workers [30-32], further studies are needed.

4 Concluding remarks

This paper presents a numerical collocation technique based on 1D-IRBFNs and Cartesian grids for the simulation of Newtonian and non-Newtonian flows in rectangular and non-rectangular domains. The technique is extremely easy to implement and capable of yielding a high level of accuracy using a relatively coarse grid. The latter is achieved owing to the facts that (i) RBFNs with the multiquadric basis function have spectral approximation power and do not require an underlying mesh (boundary points may not coincide with regular grid nodes), (ii) the problem of reduced convergence rates associated with conventional differentiation approaches is overcome, and (iii) the boundary conditions are presently implemented in an exact manner. The obtained numerical results are very encouraging, showing the great potential of the RBF collocation method in the field of computational fluid dynamics.

Acknowledgements

This work is supported by the Australian Research Council. We would like to thank the referees for their helpful comments.

References

1. Micchelli CA. Interpolation of scattered data: distance matrices and conditionally positive definite functions. *Constructive Approximation* 1986; 2:11–22.

2. Kansa EJ. Multiquadrics-A scattered data approximation scheme with applications to computational fluid-dynamics-II. Solutions to parabolic, hyperbolic and elliptic partial differential equations. *Computers and Mathematics with Applications* 1990; 19(8-9):147–161.

3. Fasshauer GE. Solving partial differential equations by collocation with radial basis functions. In: LeMhaut A , Rabut C, Schumaker LL, editors. *Surface Fitting and Multiresolution Methods*; 131–138. Nashville: Vanderbilt University Press; 1997.

4. Fasshauer GE. *Meshfree Approximation Methods With Matlab* (Interdisciplinary Mathematical Sciences - Vol. 6). Singapore: World Scientific Publishers, 2007.

5. Madych WR, Nelson SA. Multivariate interpolation and conditionally positive definite functions, II. *Mathematics of Computation* 1990; 54(189):211–230.

6. Mai-Duy N, Tran-Cong T. Approximation of function and its derivatives using radial basis function networks. *Applied Mathematical Modelling* 2003; 27:197–220.

7. Mai-Duy N, Tran-Cong T. Numerical solution of Navier-Stokes equations using multiquadric radial basis function networks. *International Journal for Numerical Methods in Fluids* 2001; 37:65–86.

8. Sarra SA. Integrated multiquadric radial basis function approximation methods. *Computers & Mathematics with Applications* 2006; 51(8):1283–1296.

9. Mai-Duy N. Solving high order ordinary differential equations with radial basis function networks. *International Journal for Numerical Methods in Engineering* 2005; 62:824–852.

10. Mai-Duy N, Tanner RI. Solving high order partial differential equations with indirect radial basis function networks. *International Journal for Numerical*

Methods in Engineering 2005; 63:1636–1654.

11. Mai-Duy N, Tran-Cong T. Solving biharmonic problems with scattered-point discretisation using indirect radial-basis-function networks. *Engineering Analysis with Boundary Elements* 2006; 30(2):77–87.

12. Ling L, Trummer MR. Multiquadric collocation method with integral formulation for boundary layer problems. *Computers & Mathematics with Applications* 2004; 48(5-6):927–941.

13. Mai-Duy N, Tanner RI. Computing non-Newtonian fluid flow with radial basis function networks. *International Journal for Numerical Methods in Fluids* 2004; 48:1309–1336.

14. Shu C, Wu YL. Integrated radial basis functions-based differential quadrature method and its performance. *International Journal for Numerical Methods in Fluids* 2007; 53(6):969–984.

15. Mai-Duy N, Khennane A, Tran-Cong T. Computation of laminated composite plates using integrated radial basis function networks. *Computers, Materials & Continua* 2007; 5:63–77.

16. Mai-Duy N, Tanner RI. A collocation method based on one-dimensional RBF interpolation scheme for solving PDEs. *International Journal of Numerical Methods for Heat & Fluid Flow* 2007; 17:165–186.

17. Mai-Duy N, Tran-Cong T. A Cartesian-grid collocation method based on radial-basis-function networks for solving PDEs in irregular domains. *Numerical Methods for Partial Differential Equations* 2007; 23:1192–1210.

18. Ghia U, Ghia KN, Shin CT. High-Re solutions for incompressible flow using the Navier-Stokes equations and a multigrid method. *Journal of Computational Physics* 1982; 48:387–411.

19. Botella O, Peyret R. Benchmark spectral results on the lid-driven cavity flow. *Computers & Fluids* 1998; 27(4):421–433.

20. Bruneau C-H, Jouron C. An efficient scheme for solving steady incompressible Navier-Stokes equations. *Journal of Computational Physics* 1990; 89(2):389–413.

21. Ostrach S. Natural convection in enclosures. *Journal of Heat Transfer* 1988; 110:1175–1190.

22. Zhu YD, Shu C, Qiu J, Tani J. Numerical simulation of natural convection between two elliptical cylinders using DQ method. *International Journal of Heat and Mass Transfer* 2004; 47(4):797–808.

23. Lee JH, Lee TS. Natural convection in the annuli between horizontal confocal elliptic cylinders. *International Journal of Heat and Mass Transfer* 1981; 24(10):1739–1742.

24. Schreiber WC, Singh SN. Natural convection between confocal horizontal elliptical cylinders. *International Journal of Heat and Mass Transfer* 1985; 28(4):807–822.

25. Elshamy MM, Ozisik MN, Coulter JP. Correlation for laminar natural convection between confocal horizontal elliptical cylinders. *Numerical Heat Transfer, Part A: Applications* 1990; 18:95–112.

26. Kamal MR, Ryan ME. Models of material behavior. In: Tucker CL, editor. *Fundamentals of Computer Modelling for Polymer Processing.* Munich: Hanser Publishers, 1989.

27. Gervang B, Larsen PS. Secondary flows in straight ducts of rectangular cross section. *Journal of Non-Newtonian Fluid Mechanics* 1991; 39:217–237.

28. Xue S-C, Phan-Thien N, Tanner RI. Numerical study of secondary flows of viscoelastic fluid in straight pipes by an implicit finite volume method. *Journal of Non-Newtonian Fluid Mechanics* 1995; 59:191–213.

29. Mai-Duy N, Tran-Cong T. A multidomain integrated radial basis function collocation method for elliptic problems. *Numerical Methods for Partial Differential Equations* 2008; 24:1301–1320.

30. Kohno H, Bathe K-J. A nine-node quadrilateral FCBI element for incompressible fluid flows. *Communications in Numerical Methods in Engineering* 2006; 22:917–931.

31. Kohno H, Bathe K-J. A flow-condition-based interpolation finite element procedure for triangular grids. *International Journal for Numerical Methods in Fluids* 2006; 51:673–699.

32. Banijamali, B, Bathe, K-J. The CIP method embedded in finite element discretizations of incompressible fluid flows. *International Journal for Numerical Methods in Engineering* 2007; 71:66–80.

Table 1: Lid-driven cavity flow, $Re = 1000$: Extrema of the vertical and horizontal velocity profiles through the centre of the cavity. The results obtained by the pseudo spectral method and FDM are also included for comparison.

Method	Density	u_{min}	Error %	y	v_{max}	Error %	x	v_{min}	Error %	x
Present	21×21	-0.25784	33.643	0.200	0.26633	29.345	0.190	-0.36691	30.387	0.858
	31×31	-0.34791	10.464	0.187	0.33580	10.913	0.168	-0.46765	11.274	0.898
	41×41	-0.37122	4.466	0.177	0.35910	4.733	0.162	-0.50168	4.818	0.906
	51×51	-0.37985	2.245	0.174	0.36781	2.421	0.160	-0.51469	2.350	0.908
	61×61	-0.38366	1.263	0.173	0.37173	1.382	0.159	-0.52029	1.288	0.909
	71×71	-0.38560	0.764	0.172	0.37375	0.846	0.159	-0.52306	0.762	0.909
	81×81	-0.38669	0.484	0.172	0.37490	0.541	0.158	-0.52458	0.475	0.909
	91×91	-0.38733	0.320	0.172	0.37558	0.360	0.158	-0.52545	0.309	0.909
	101×101	-0.38772	0.218	0.172	0.37601	0.247	0.158	-0.52598	0.208	0.909
FDM($\psi - \omega$) [18]	129×129	-0.38289	1.462	0.172	0.37095	1.589	0.156	-0.51550	2.197	0.906
FDM($\mathbf{u} - p$) [20]	256×256	-0.3764	3.132	0.160	0.3665	2.770	0.152	-0.5208	1.192	0.910
Benchmark [19]		-0.38857		0.172	0.37694		0.158	-0.52708		0.909

Table 2: Lid-driven cavity flow, $Re = 1000$, Primary vortex: Intensities. The results obtained by the pseudo spectral method and FDM are also included for comparison.

Method	Density	ψ_{min}	Error %	ω	Error %	x_1	x_2
Present	21×21	-0.08886	25.286	-1.75452	15.148	0.531	0.600
	31×31	-0.10780	9.363	-1.92140	7.077	0.533	0.570
	41×41	-0.11419	3.996	-2.00322	3.120	0.532	0.567
	51×51	-0.11653	2.029	-2.03463	1.601	0.532	0.566
	61×61	-0.11756	1.156	-2.04886	0.913	0.531	0.566
	71×71	-0.11810	0.707	-2.05623	0.557	0.531	0.565
	81×81	-0.11840	0.451	-2.06062	0.344	0.531	0.565
	91×91	-0.11858	0.300	-2.06308	0.225	0.531	0.565
	101×101	-0.11869	0.206	-2.06461	0.151	0.530	0.565
FDM($\psi - \omega$) [18]	129×129	-0.11793	0.849	-2.04968	0.874	0.531	0.563
FDM($\mathbf{u} - p$) [20]	256×256	-0.1163	2.220	—	—	0.531	0.559
Benchmark [19]	—	-0.11894		-2.06775		0.531	0.565

Table 3: Natural convection, $Ra = 10^4$, $P_r = 0.71$, $rr = 2.6$, $e_i = 0.5$, $e_o = 0.5$: Average Nusselt number. The grid independent value of $\overline{N_u}$ obtained by the DQ method is also included for comparison.

Grid	37×37	41×41	47×47	51×51	57×57	Zhu et al [22]
$\overline{N_u}$	3.21	3.21	3.22	3.22	3.22	3.25

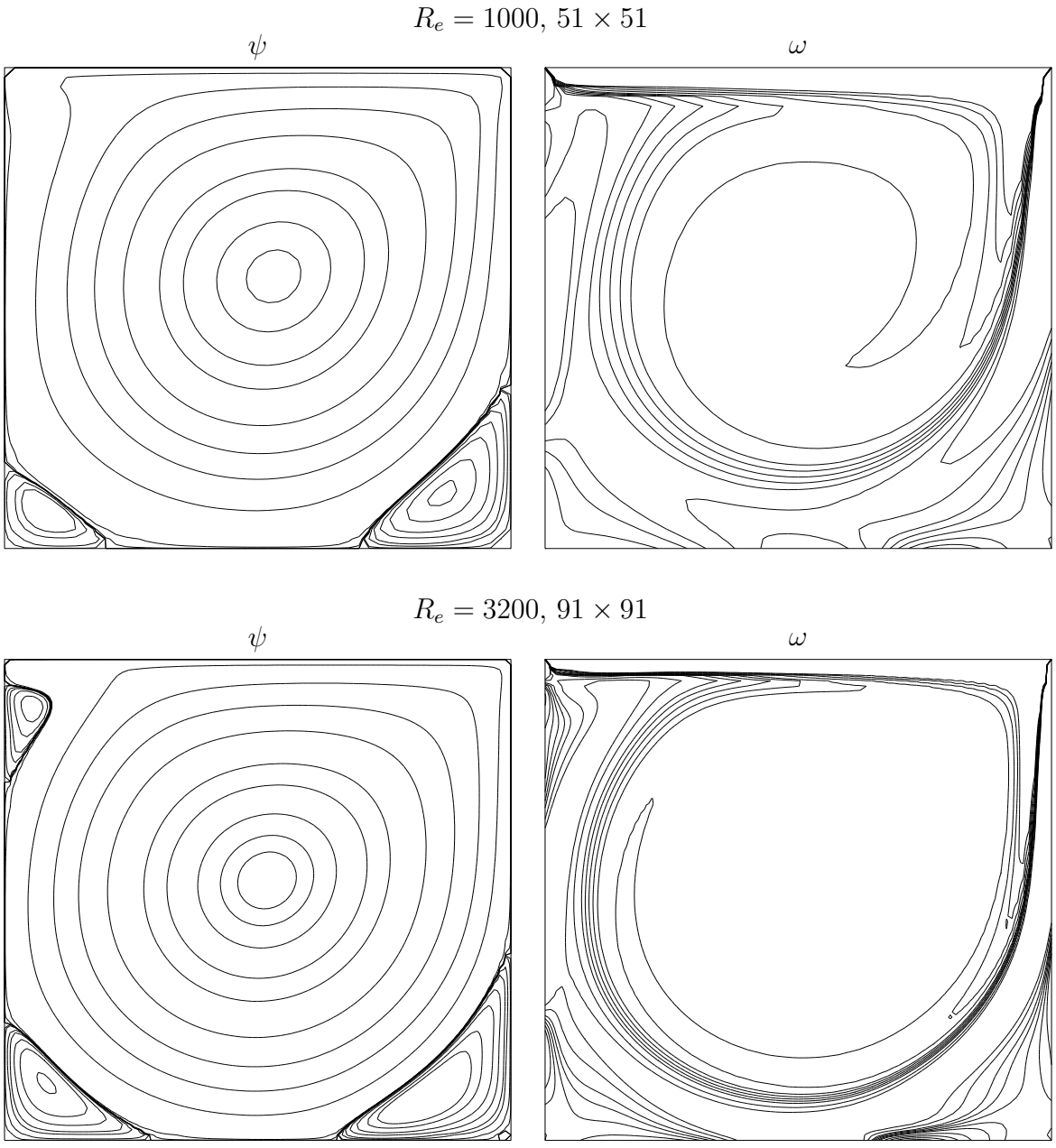

Figure 1: Lid-driven cavity flow: stream and iso-vorticity lines. The contour values used here are taken to be the same as those in [19].

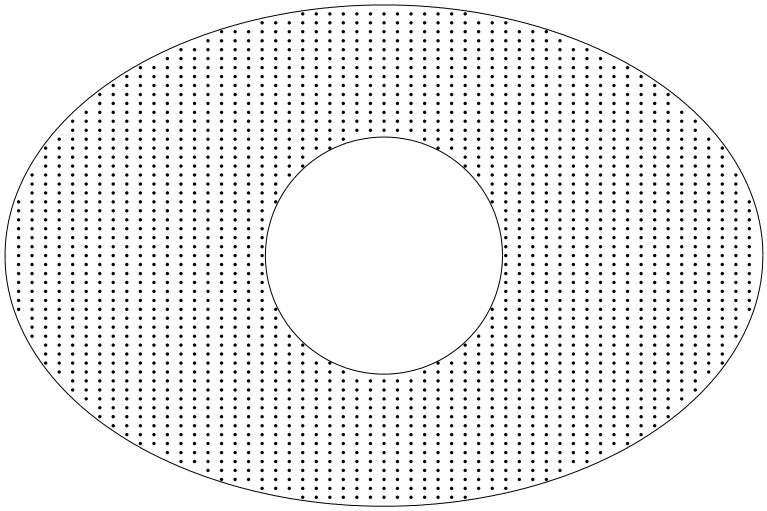

Figure 2: Natural convection flow: discretisation.

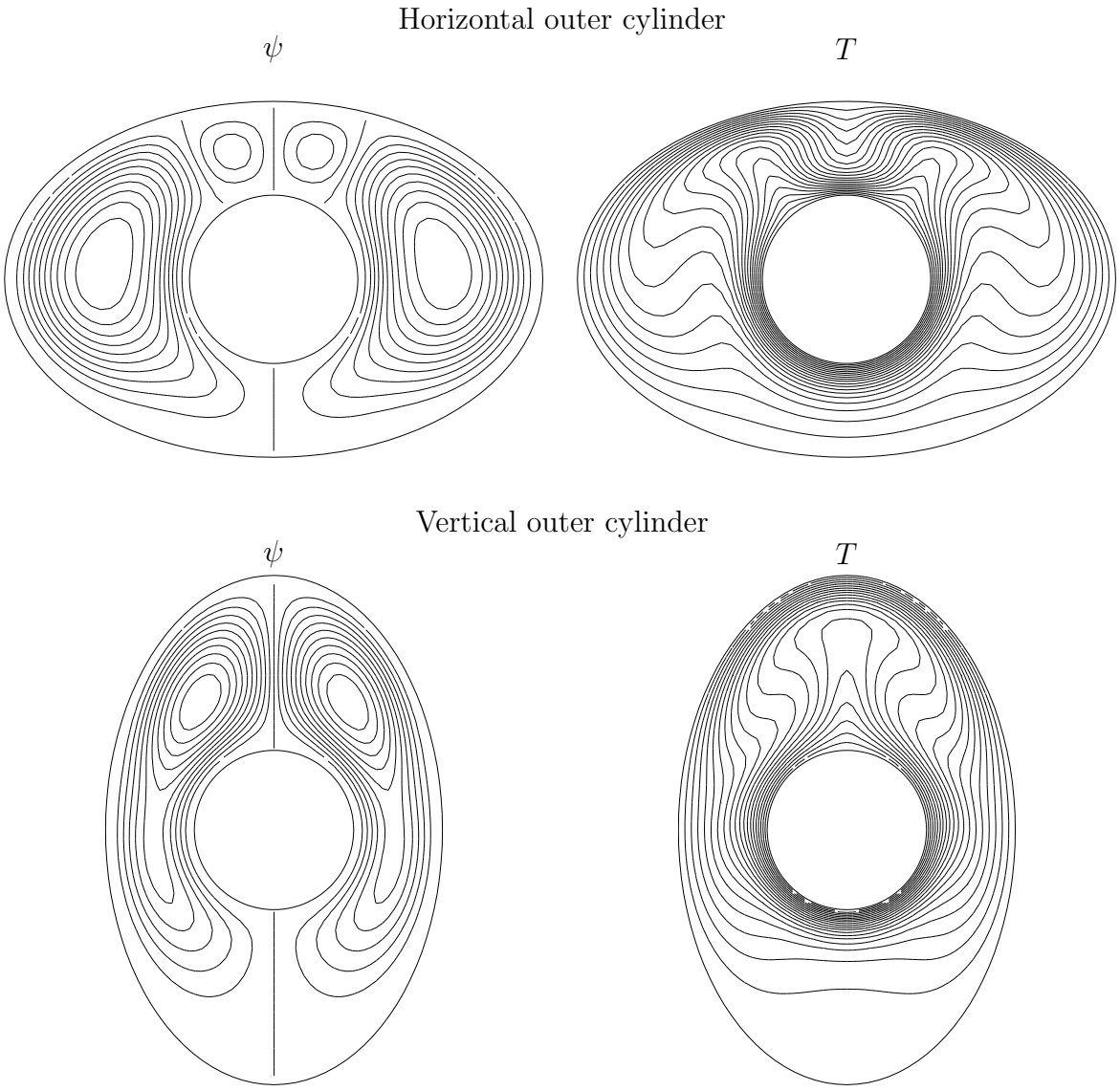

Figure 3: Natural convection flow, $R_a = 10^4$, $e_i = 0$, $e_o = 0.75$, 57×57: streamlines and isotherms. Each plot contains 21 contour lines whose values vary linearly between the extremes.

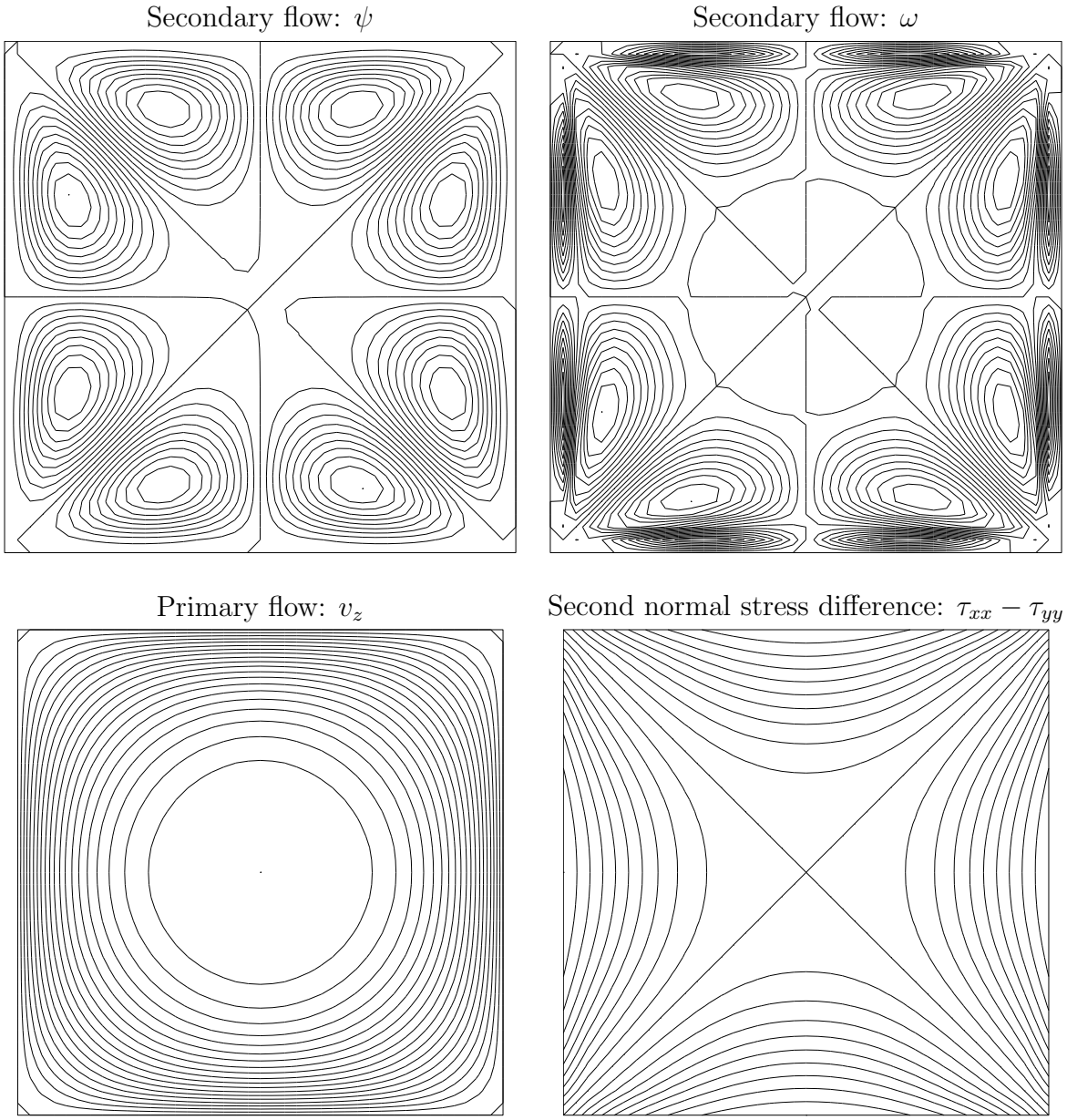

Figure 4: Viscoelastic flow in a straight pipe of square cross section, 41×41, relaxation factor of 0.005: contour plots for some primary quantities. Each plot contains 21 contour lines whose values vary linearly between the extremes.